PERGAMON

International Journal of Heat and Mass Transfer 44 (2001) 2541–2553

International Journal of HEAT and MASS TRANSFER

www.elsevier.com/locate/ijhmt

Heat transfer and fluid flow in a high-intensity free-burning arc: an improved modeling approach

Xi Chen *, He-Ping Li

Engineering Thermophysics Division, Department of Engineering Mechanics, Tsinghua University, Beijing 100084, People's Republic of China

Received 26 June 2000

Abstract

The high-intensity free-burning arc is modeled using a computational domain including the arc itself and the arc cathode and anode. It is shown that the energy equation with the temperature, instead of the specific enthalpy, as the dependent variable has to be used in order to obtain physically reasonable heat fluxes from the plasma to the electrodes if a SIMPLE-like algorithm is employed in the modeling. New difficulty encountered in the numerical solution of the energy equation is discussed in some detail and has been overcome successfully by use of a 'pseudo-density' method and a deferred-correction discretization scheme. A more realistic boundary condition is adopted at the rear face of the anode plate for the solution of the potential equation in order to reveal the effect of electrical collection at the anode on the current density and temperature distributions within the anode plate. Special treatments at the plasma–electrode interfaces are also discussed and adopted in the modeling.

1. Introduction

The high-intensity free-burning arc is an idealized representative of the DC arcs encountered in many applications (e.g., in gas-tungsten welding, in transferred arc furnaces, in DC plasma torches, etc.). It can be studied experimentally under well-controlled conditions (e.g., the gas composition, gas pressure and electrode cooling can be well controlled), and its axi-symmetry can also facilitate the modeling work and the comparison of the predicted arc characteristics with corresponding experimental data. Numerous papers have been published in the last two decades to model the free-burning arc along with experimental investigations.

Modeling of the high-intensity free-burning arc involves complicated interactions between the electromagnetic field and the arc self-induced fluid flow and heat transfer, and thus represents a rather difficult task. Hsu et al. [1] first overcame successfully the difficulty in computing the unknown electromagnetic fields and the plasma flow induced by the arc itself, and gave detailed modeling results concerning the fluid flow and heat transfer within the high-intensity free-burning arc. Two-dimensional (axi-symmetrical) continuity, momentum and energy conservation equations and electrical potential (or current continuity) equation were simultaneously solved using the finite-difference method and the SIMPLE algorithm described by Patankar [2]. Predicted isotherms were shown to be in reasonable agreement with corresponding experimental data. In order to avoid the difficulty related to the complex physical phenomena in the plasma sheaths close to the electrode surfaces, the computational domain used in their modeling for the solution of electrical potential equation did not include the arc cathode and anode. Instead, an exponential distribution of the axial component of current density was assumed on the plane perpendicular to the arc axis and across the cathode tip. And a measured temperature profile (the temperatures are high enough to ensure the arc current passage) was employed along the outer edge of the boundary layer on the anode surface. Their modeling approach was followed in many subsequent studies (e.g., [3–5]) and was also used in the modeling of the transferred arc (e.g., [6]) or the DC arc

* Corresponding author. Tel.: +86-10-6277-2924; fax: +86-10-6278-1824.

E-mail address: cx-dem@mail.tsinghua.edu.cn (X. Chen).

0017-9310/01/$ - see front matter
PII: S0017-9310(00)00290-8

Nomenclature

B_θ	circumferential component of the self-induced magnetic induction intensity
C_p	specific heat at constant pressure
e	elementary charge
E_i	ionization potential of the gas
h	specific enthalpy
H	distance between two cirques
I	arc current
j	local current density
j_e, j_i	electron current density, ion current density
j_r, j_x	radial and axial components of the current density vector
j_R	thermionic current density
j_0	a uniform current density at the upstream end of the cathode
k	thermal conductivity of the gas
k_B	Boltzmann constant
m_i	ion mass
n_i	number density of ions
p	pressure of the gas
q_c	additional energy flux at the cathode surface
$q_{r,a}$	local radiation heat flux from the bulk plasma to anode surface
$q_{r,c}$	local radiation heat flux from the bulk plasma to cathode surface
q_s	heat flux across the plasma–anode interface
r, x	radial and axial coordinates
r_c	radius of the cathode rod
R_i $(i = 1, 2, 3, 4)$	radius of the ith cirque
S_Φ	source term
S_R	radiation power per unit volume of the gas
T	temperature
T_w	wall temperature
u, v	axial and radial velocity components
$\mathbf{U}$	velocity vector
V_a, V_c	anode potential drop, cathode potential drop
$\bar{v}_i$	mean thermal speed of ions
W_s	work function of material
X_{12}	angle factor

Greek symbols

Φ	any scalar variable to be solved
Γ	diffusion coefficient
α	Stefan–Boltzmann constant
ϵ_a, ϵ_c	anode emissivity, cathode emissivity
ϕ	electrical potential
λ	blending factor
μ	gas viscosity
ρ	mass density
σ	electrical conductivity

Subscripts

a	anode
c	cathode
e	electrons
g	gas
i	ions
r	radiation
s	interface
w	western interface of the control volume or wall

Superscripts

u	upwind discretization scheme
c	central-difference discretization scheme

plasma torch (e.g., [7]). Refs. [7,8] used a uniform current density profile across the electron-emitting region at a flat cathode surface instead of the exponential profile employed by Hsu et al. [1]. It is obvious that using an assumed current density distribution at the cathode tip plane and using a measured temperature profile outside the anode boundary layer make those modeling approaches being somewhat empirical.

As an important improvement, subsequent studies include the cathode and/or the anode in the computational domain. This approach is more reasonable because some of empirical treatments used in the previous studies (e.g., the choice of the radius of the electron-emitting region or the parameter in the current density profile) can be removed. The thin plasma sheaths close to the electrodes are often ignored, but some additional treatments at the plasma–electrode interfaces are usually required. The cathode was included in the computational domain by the authors of Refs. [9–14]. In their studies, the uniform current density was assumed at the upstream end of the cathode (equal to the input arc current divided by the cross-sectional area of the cathode rod). If some physical processes at the arc anode (e.g., melting and evaporation of anode material) were important, it would be better to include the anode plate in the computational domain [6,15,16]. Both the arc cathode and anode plate have thus been included in the computational domain in the studies of Refs. [17–19].

However, available studies are not quite satisfactory even if the approach including both the arc cathode and anode in the computational domain is employed in the modeling. For example, so far almost all the researchers used the energy equation with the specific enthalpy as the dependent variable and solved it in coupling with the continuity, momentum and potential equations using a SIMPLE-like (SIMPLE, SIMPLER or SIMPLEC) algorithm [2,20]. As we see later on, such an approach cannot give physically reasonable heat fluxes from the plasma to the electrodes. In addition, zero potential condition was always employed at the rear face of the anode in all those studies for the solution of the electrical potential equation. This boundary condition is often not represent the realistic case of the electrical collection at the anode. Usually the rear face of arc anode used in an experiment is centrally water-cooled, and thus the arc current flows only through part of the rear face of the anode plate. The condition of the electrical collection at the anode surface may affect appreciably the current density distribution and thus affect the temperature field within the arc anode [21,22]. It is expected that this effect will be important when melting and/or evaporation of the anode material are involved.

Keeping those problem points of available studies in mind, this paper aims at presenting an improved approach for modeling of the high-intensity free-burning arc. The computational domain will include the arc itself and the arc anode and cathode. The energy equation with the temperature as the dependent variable will be used, and a more realistic potential condition at the rear face of the anode plate will be adopted.

2. Modeling approach

2.1. Assumptions

The assumptions used in the present modeling include: (1) the plasma is optically thin and is in local thermodynamic equilibrium (LTE) state; (2) the plasma flow is steady, laminar and axi-symmetrical; and (3) the gravity, the viscous dissipation and the pressure work are negligible.

2.2. Governing equations

The following continuity and momentum equations in the cylindrical coordinates are used in this work:

$$\frac{\partial}{\partial x}(\rho u)+\frac{1}{r}\frac{\partial}{\partial r}(r\rho v)=0, \tag{1}$$

$$\frac{\partial}{\partial x}(\rho uu)+\frac{1}{r}\frac{\partial}{\partial r}(r\rho uv)=-\frac{\partial p}{\partial x}+2\frac{\partial}{\partial x}\left(\mu\frac{\partial u}{\partial x}\right)+\frac{1}{r}\frac{\partial}{\partial r}\left[r\mu\left(\frac{\partial u}{\partial r}+\frac{\partial v}{\partial x}\right)\right]+j_{\mathrm{r}}B_{\theta}, \tag{2}$$

$$\frac{\partial}{\partial x}(\rho uv)+\frac{1}{r}\frac{\partial}{\partial r}(r\rho vv)=-\frac{\partial p}{\partial r}+\frac{\partial}{\partial x}\left[\mu\left(\frac{\partial v}{\partial x}+\frac{\partial u}{\partial r}\right)\right]+\frac{2}{r}\frac{\partial}{\partial r}\left(r\mu\frac{\partial v}{\partial r}\right)-\frac{2\mu v}{r^2}-j_{\mathrm{x}}B_{\theta}. \tag{3}$$

In these equations, u and v are the axial and radial velocity components, p the gas pressure, whereas ρ and μ are the temperature-dependent gas density and viscosity, respectively. j_{x} and j_{r} are the axial and radial components of the current density vector. B_{θ} is the circumferential component of the self-induced magnetic induction intensity due to the arc current, and is calculated by

$$B_{\theta}=\frac{\mu_0}{r}\int_0^r j_{\mathrm{x}}\xi\,\mathrm{d}\xi \tag{4}$$

in which μ_0 is the permeability in vacuum. The electrical potential or current continuity equation is

$$\frac{\partial}{\partial x}\left(\sigma\frac{\partial\phi}{\partial x}\right)+\frac{1}{r}\frac{\partial}{\partial r}\left(r\sigma\frac{\partial\phi}{\partial r}\right)=0 \tag{5}$$

in which σ is the electrical conductivity. ϕ is the electrical potential and is related to the current density components j_{x} and j_{r} by $j_{\mathrm{x}}=-\sigma\partial\phi/\partial x$ and $j_{\mathrm{r}}=-\sigma\partial\phi/\partial r$. Differently from the previous studies, the following energy equation with the temperature T as the dependent variable is used in the present modeling:

$$\frac{\partial\left(\rho uC_{\mathrm{p}}T\right)}{\partial x}+\frac{\partial\left(r\rho vC_{\mathrm{p}}T\right)}{r\partial r}=\frac{\partial}{\partial x}\left(k\frac{\partial T}{\partial x}\right)+\frac{1}{r}\frac{\partial}{\partial r}\left(kr\frac{\partial T}{\partial r}\right)+\frac{j_{\mathrm{x}}^2+j_{\mathrm{r}}^2}{\sigma}-S_{\mathrm{R}}+\frac{5}{2}\times\frac{k_{\mathrm{B}}}{e}\left(j_{\mathrm{x}}\frac{\partial T}{\partial x}+j_{\mathrm{r}}\frac{\partial T}{\partial r}\right)+T\left[\frac{\partial\left(\rho uC_{\mathrm{p}}\right)}{\partial x}+\frac{\partial\left(r\rho vC_{\mathrm{p}}\right)}{r\partial r}\right], \tag{6}$$

where k, C_{p} and S_{R} are the temperature-dependent gas thermal conductivity, specific heat at constant pressure and radiation power per unit volume of plasma. k_{B} is the Boltzmann constant, whereas e is the elementary charge.

2.3. Computational domain and boundary conditions

Fig. 1 shows the computational domain used in the present modeling, which includes the cathode rod, the anode plate and the arc itself and carries the related geometrical sizes. The radial dimension of the domain is taken to be large enough so that zero u and v can be used at the outer boundary of the computational domain (CE). Boundary conditions used in the present modeling have been given in Table 1. Because most of them are usual, here only a brief discussion is given for the boundary conditions of the electrical potential equation. At the upstream end of the cathode (FG), a uniform current density equal to $j_{\mathrm{x}}=j_0=I/\left(\pi r_{\mathrm{c}}^2\right)$ (I is the arc current, whereas r_{c} is the radius of the cathode rod) is

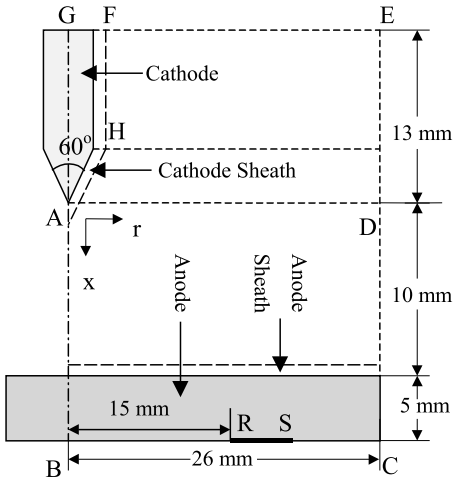

Fig. 1. Computational domain and geometrical sizes used in this study.

taken. Because usually not the whole rear face of the anode plate is used as for the current passage in actual experimental setups (e.g., in [1]), $\phi = 0$ is not always the appropriate condition along BC. In this study, ϕ is set to be zero for the segment acting as the arc current passage (RS), whereas $\partial\phi/\partial x = 0$ is used for the other part of BC. Zero normal derivative of potential is also used for all other boundaries.

2.4. Discussion concerning the energy equation

Since the energy equation employed in the present modeling, i.e., Eq. (6), is different from that used by the many previous authors, it seems necessary to discuss it in some detail. The previous studies used the SIMPLE-like algorithm to solve the governing equations and used the following form of energy equation with specific enthalpy as the dependent variable in the modeling.

$$\frac{\partial}{\partial x}(\rho u h) + \frac{1}{r}\frac{\partial}{\partial r}(r\rho v h) = \frac{\partial}{\partial x}\left(\frac{k}{C_p}\frac{\partial h}{\partial x}\right) + \frac{1}{r}\frac{\partial}{\partial r}\left(r\frac{k}{C_p}\frac{\partial h}{\partial r}\right) + \frac{j_x^2 + j_r^2}{\sigma} - S_R + \frac{5}{2}\frac{k_B}{e}\left(j_x\frac{1}{C_p}\frac{\partial h}{\partial x} + j_r\frac{1}{C_p}\frac{\partial h}{\partial r}\right). \quad (7)$$

The merit of using energy equation (7) is that its form is in complete consistence with the following general differential equation handled by the SIMPLE-like algorithm (cf. Patankar [2]) and thus facilitate programming:

$$\nabla\cdot(\rho\mathbf{U}\Phi) = \nabla\cdot(\Gamma\nabla\Phi) + S_\Phi. \quad (8)$$

In Eq. (8), ρ is the fluid density, $\mathbf{U}$ the velocity vector, Γ the 'diffusion coefficient', S_Φ the source term, whereas Φ is any scalar variable to be solved in the computation. However, Eq. (7) is not suitable for the solution of a conjugate conduction–convection problem if temperature-dependent fluid specific heats are involved in the computation [23]. For the present case including the arc anode and cathode in the computational domain, we do meet such a conjugate heat transfer problem. Namely, the heat conduction within the solid electrodes is coupled with the convection heat transfer from the plasma region, and the gas specific heat varies significantly with the plasma temperature. Eq. (7) is thus not an appropriate energy equation to be employed in the modeling. The reason can be further clarified as follows. Firstly, we meet a difficulty about how to define consistently the specific enthalpy h in the plasma region and in the electrode regions to ensure the continuity of both the temperature and the specific enthalpy at the plasma–electrode interfaces. Secondly, even if we can find a way to resolve the problem about how to define the enthalpy in the solid regions, we still meet another difficulty, i.e., the computed heat flux across the plasma–electrode interface (e.g., across the plasma–anode interface) will be physically incorrect. In the following this problem point will be discussed in more detail for the plasma–anode interface. The same discussion is also applicable to the plasma–cathode interface. As is well known, when the SIMPLE-like algorithm [2] is employed and when Eq. (7) is discretized across the plasma–anode interface, the heat flux across the plasma–anode interface will be calculated by

$$q_s = -\left(k/C_p\right)_s(\Delta h/\Delta x), \quad (9)$$

where Δx is the axial distance between the two adjacent grid points across the plasma–anode interface (i.e., between the grid points nearest to the interface but located respectively, in the anode side and in the plasma side),

Table 1
Boundary conditions for governing equations along the boundaries shown in Fig. 1

	GB	BC	CE	EF	FG
u	$\partial u/\partial r = 0$	$u = 0$	$u = 0$	$u = 0$	$u = 0$
v	$v = 0$	$v = 0$	$v = 0$	$v = 0$	$v = 0$
T	$\partial T/\partial r = 0$	$T = 500$ K RS : $\phi = 0$	$T = 500$ K	$T = 500$ K	$T = 1000$ K
ϕ	$\partial\phi/\partial r = 0$	Else : $\partial\phi/\partial x = 0$	$\partial\phi/\partial r = 0$	$\partial\phi/\partial x = 0$	$-\sigma\partial\phi/\partial x = j_0$

whereas Δh is the enthalpy difference between the two grid points. $(k/C_p)_s$ is the value of 'diffusion coefficient' at the interface and is calculated by the harmonic mean of the values of (k/C_p) at the two grid points [2]. When uniform grid spacing is used, $(k/C_p)_s$ will be expressed as

$$\left(\frac{k}{C_p}\right)_s = \frac{2(k/C_p)_g(k/C_p)_a}{(k/C_p)_g + (k/C_p)_a} \tag{10}$$

in which $(k/C_p)_g$ and $(k/C_p)_a$ are the values of (k/C_p) (the ratio of thermal conductivity to specific heat) in the plasma side (g) and in the anode side (a). After substituting $(k/C_p)_s$ calculated by Eq. (10) into Eq. (9), it is obvious that the heat flux q_s across the plasma–anode interface will depend on the specific heat of the anode material ($C_{p,a}$). However, because now only steady heat conduction occurs in the anode region, the heat flux within the anode or at the plasma–anode interface should be independent of the specific heat of the anode material, and thus the calculated heat flux by Eq. (9) is physically incorrect. This is the main reason why we consider that the energy equation (7) with the specific enthalpy as the dependent variable should be abandoned and the energy equation (6) with the temperature as the dependent variable should be employed in the modeling. Using Eq. (6), instead of Eq. (7), in the modeling can avoid all the difficulties mentioned above. For this case, we no longer need to pay attention to the consistent definition of the specific enthalpy in the plasma region and in the electrode regions, and the heat flux across the plasma–anode interface will be calculated by

$$q_s = -k_s(\Delta T/\Delta x) \tag{11}$$

in which k_s is the harmonic mean of k_g and k_a. Note that here q_s is no longer dependent on the specific heat of solid material and thus a physically reasonable heat flux from the plasma to the anode surface can be naturally obtained.

Nevertheless, when the energy equation with the temperature as the dependent variable, i.e., Eq. (6), is employed, one may also meet some other problems for its solution. Firstly, it is noted that Eq. (6) is not completely consistent with the general differential equation (8) handled by the standard SIMPLE-like algorithm [2]. If Φ in Eq. (8) is taken to be temperature T, ρC_p (the product of fluid density and specific heat) should be used to substitute the fluid density ρ in the general equation (8) in order to be consistent with Eq. (6). Ignoring this special feature of Eq. (6) would result in a serious mistake if the SIMPLE-like algorithm is still employed in the computation. In our computation, this problem is resolved using the so-called 'pseudo-density' method [23] as follows. When Eq. (6) is solved in each round of iterations to solve simultaneously the governing equations, a 'pseudo-density' equal to ρC_p is temporarily used as the substitute of ρ in the general equation (8) (with $\Phi = T$ and $\Gamma = k$). After the energy equation has been solved, actual fluid density ρ is re-used for solving other equations.

An important finding in this study is that the usual approach employing the power-law scheme to discretize the combined convection and diffusion term [2] cannot be employed to solve the present energy equation (6). It is found from the computation that if the power-law scheme usually employed in the previous studies is still used to discretize Eq. (6), convergent computational results always cannot be obtained. The reason for this puzzling phenomenon to appear is as follows. Eq. (6) is seen to be completely equivalent to Eq. (7) since $dh = C_p\ dT = d(C_pT) - T\ dC_p$ or $\Delta h = \Delta(C_pT) - T\Delta C_p$ in the difference form. However, for many thermal plasmas $\Delta(C_pT)$ or $T\Delta C_p$ is often much greater than Δh. Table 2 gives some typical calculated results for an argon plasma concerning $\Delta h, \Delta(C_pT)$ and $T\Delta C_p$ for several different plasma temperatures. In the calculation, the temperature difference $\Delta T = 50$ K is assumed. As is seen from Table 2, $\Delta(C_pT)$ or $T\Delta C_p$ is about one order of magnitude greater than Δh. Hence, when different discretization schemes are respectively used for the terms $\nabla(C_pT)$ and $T\nabla C_p$ (e.g., the power-law scheme is used for $\nabla(C_pT)$ appearing in the combined convection-diffusion term, while central difference scheme is used for $T\nabla C_p$ appearing in the source term of Eq. (6)), the error caused by the different discretization schemes may significantly exceed the term Δh itself and thus results in an incorrect computational result. This trouble can be avoided only by using the same discretization scheme for both $\nabla(C_pT)$ and $T\nabla C_p$.

In our computation, the central-difference scheme has been employed to discretize all the convection term, the diffusion term and the source term of Eq. (6). For the sake of numerical stability, the convective term is discretized in a deferred-correction way [24,25]. For example, the convection term at the western interface (w) of the control volume is discretized as

$$(\rho u C_p T)_w^{n+1} = (\rho u C_p T)_w^{u,n+1} + \lambda\lfloor(\rho u C_p T)_w^{c,n} - (\rho u C_p T)_w^{u,n}\rfloor, \tag{12}$$

Table 2
Typical calculated results of $\Delta h, \Delta(C_pT)$ and $T\Delta C_p$ for several plasma temperatures (argon plasma at the LTE state and atmospheric pressure; temperature difference $\Delta T = 50$ K is adopted for the difference calculation)

T (K)	Δh	$\lvert\Delta(C_pT)\rvert$	$\lvert T\Delta C_p\rvert$
12 000	0.23×10^6	0.16×10^7	0.14×10^7
13 000	0.36×10^6	0.21×10^7	0.17×10^7
14 000	0.46×10^6	0.14×10^7	0.90×10^6
15 000	0.46×10^6	0.59×10^6	0.11×10^7
16 000	0.35×10^6	0.18×10^7	0.21×10^7
17 000	0.23×10^6	0.15×10^7	0.17×10^7

where the superscripts u and c express respectively, the upwind and central-difference discretization schemes, and n and $n+1$ represent, respectively, the nth and the $(n+1)$th iteration levels. The parameter λ blends the two schemes with the limiting values $\lambda = 0$ for the upwind scheme and $\lambda = 1$ for the central-difference scheme. The value of λ has been taken to be 0.9 or even 1.0 (at convergence) in the computation. It is noted from Eq. (12) that for the $(n+1)$th iteration level, the convection term of Eq. (6) is discretized actually by the upwind scheme because the correction term $\lambda[(\rho u C_p T)_w^{c,n} - (\rho u C_p T)_w^{u,n}]$ is calculated by the quantities in the nth iteration level and thus treated as a part of the source terms. Hence, the deferred-correction scheme always leads to a diagonally dominant coefficient matrix, and thus ensures the necessary numerical stability. On the other hand, the central-difference discretization scheme is actually employed at convergence and thus a high-order accuracy of the solution can be achieved for the energy equation. It is found that a convergent solution indeed can been obtained by employing this approach to discretize the energy equation (6).

2.5. Special treatments at plasma–electrode interfaces

96 (x-direction) × 76 (r-direction) grid points have been employed in the present modeling. The conical part of the cathode is approximated by a series of rectangular steps [2], and thus the cathode tip becomes a small cylinder with height of 0.2 mm and radius of 0.1 mm. Plasma sheaths close to the electrodes are ignored in this study. Instead, a special treatment similar to that used in [13] has been employed at the cathode. Namely, the distance between the frontal surface of the cathode tip and the nearest grid point in the plasma side is taken to be 0.1 mm. Since the plasma temperature at the grid point near the cathode tip is comparatively high, corresponding value of the plasma electrical conductivity at this point is great enough. Hence, the harmonic mean of this value of the electrical conductivity of the plasma and that of the cathode material can ensure the current passage. Similarly, the distance between the anode surface and the nearest grid point in the plasma side is also taken to be 0.1 mm to ensure the current passage from the plasma to the anode near the arc axis.

Similar to but somewhat different from the previous studies [18,19], additional treatments have been employed at the plasma–electrode interfaces in the present modeling. The current continuity in the cathode region can be analyzed as follows. Firstly, only free electrons can flow within the cathode rod, and thus $j_e = j$ must hold true there. Here j is the net local current density at any location within the cathode rod, whereas j_e is the local electron current density at the same location. Secondly, if we assume the thermionic emission is the only mechanism for the electron release from the cathode and the thermionic current density is denoted by j_R, j_R will consist of two groups of electrons. The first group includes the electrons that release from the cathode and recombine with incident ions at the cathode surface (this part of j_R is equal to j_i), whereas the second group includes all the other electrons that leave from the cathode and enter the plasma (this part of j_R, or $j'_e = j_R - j_i$, is equal to $j - j_i$). Hence, the physical condition $j = j_R$ can be used at the cathode surface. The current density due to the thermionic emission, j_R, is calculated by the Richardson–Dushman formula (Condon and Odishaw [26]) as

$$j_R = 1.16 \times 10^6 T_w^2 \exp\left(-\frac{eW_{s,c}}{k_B T_w}\right) \tag{13}$$

in which $W_{s,c}$ is the work function of the cathode material (tungsten). The local ion current density j_i incident to the cathode surface from the plasma is evaluated by $j_i = (1/4)en_i\bar{v}_i = (1/4)en_i[8k_BT/(\pi m_i)]^{1/2}$, where m_i, n_i and $\bar{v}_i$ are the ion mass, number density and mean thermal speed, whereas T is the plasma temperature at the grid point nearest to the cathode surface. All the ions arriving at the cathode surface are assumed to recombine at the cathode surface with electrons released from the cathode, and the atoms formed in the electron–ion recombination process will return to the bulk plasma. After considering the electron–ion recombination at the cathode surface, the net electron current density entering the plasma will be $j'_e = j_R - j_i$. Since the net current in the plasma side consists of the electron current and the ion current, i.e., $j = j'_e + j_i$, the physical condition $j = j_R$ is obtained again on the plasma side. In the present model, the contribution of electrons coming from the bulk plasma to the local current density at the cathode surface has been ignored. It is because that only few electrons with very high kinetic energy can overcome the repulsive potential barrier (for electrons) and arrive at the cathode surface.

In our computation, firstly j is calculated at the cathode tip from the solution of the electrical potential equation (5). Then the local electron current density due to the thermionic emission j_R is thus obtained from the physical condition $j_R = j$, and the local cathode-surface temperature (T_w) can be calculated by means of Eq. (13).

It is noticed that here we have employed a definition of the thermionic emission current density (j_R), which is different from that used by many previous authors. For example, Lowke et al. [19] defined the net electron current density entering the plasma (i.e., $j'_e = j_R - j_i$ mentioned above) as the thermionic emission current density (j_r). Although Eq. (13) are used by us and by those authors to calculate the thermionic emission current density (j_R or j_r), different values of the work function

should be employed in the calculation. Lowke et al. [19] suggested that the local current density j and the thermionic current density j_r at a given surface temperature are respectively calculated at first. They employed $j_i = j - j_r$ for the case with $j \geqslant j_r$, whereas $j_i = 0$ for the case with $j < j_r$. Physically, it is expected that the ion current j_i always exists due to the driving by the attractive electric field (for ions) near the cathode, and the maintenance of high cathode-surface temperature relies, to a considerable degree, on the ion bombardment and the ion–electron recombination. Hence, the condition $j_i = 0$ used in [19] for some cases is non-reasonable. On the other hand, our j_R definition is identical to that used by Ushio et al. [27] in their measurements of the work function of cathode materials, so we can use their measured value of the work function. In our opinion, employing the present j_R definition and employing $j = j_R$ as the physical condition of current continuity at the cathode surface are more convenient and natural not only for the work function measurements [27], but also for the arc modeling.

The following additional energy flux will appear at the cathode surface:

$$q_c = q_{r,c} - \varepsilon_c \alpha T_w^4 - j_R W_{s,c} + j_i(E_i + V_c). \tag{14}$$

This energy flux, after multiplying by the surface area of the pertinent near-surface control volume and then dividing by its volume, will be added to the near-surface control volume in the cathode side as the additional source (or sink) term of the energy equation. On the right-hand side of Eq. (14), the first and second terms represent respectively, the local radiative heat flux from the bulk plasma to the cathode and the local radiation heat loss from the cathode surface to the surroundings. Here ε_c and α are the emissivity of cathode material ($\varepsilon_c = 0.3$) and the Stefan–Boltzmann constant. The third term represents the energy required for the thermionic emission, and j_R is expressed by Eq. (13). The fourth term represents the ionization energy released when the accelerated ions arrive at the cathode surface and recombine with electrons released from the surface, and E_i is the gas ionization potential (15.75 V for argon), V_c the cathode potential drop (3.0 V), whereas j_i is the ion current density mentioned above.

Similarly, the additional energy flux from the plasma to anode surface is

$$q_a = q_{r,a} + j(W_{s,a} + V_a). \tag{15}$$

After conversion by means of the method described above for the cathode surface, q_a will be added to the near-interface control volume in the anode side as an additional source term of the energy equation. On the right-hand side of Eq. (15), the first term represents the local radiative heat flux from the bulk plasma to the anode surface and $q_{r,a}$ is calculated by

$$q_{r,a} = \varepsilon_a \sum_{i,j} 2\pi U_R r_j \Delta x_i \Delta r_j X_{12} / \lfloor \pi(r_4^2 - r_3^2) \rfloor \tag{16}$$

in which U_R is the temperature-dependent radiation power per unit volume of plasma, whereas ε_a is the absorption coefficient of the anode material ($\varepsilon_a = 0.6$ is used here). X_{12} is the angle factor between the two surfaces shown in Fig. 2 and is calculated by the following expression:

$$\begin{aligned} X_{12} = \frac{1}{2(R_2^2 - R_1^2)} \Bigg[& \sqrt{\left(R_2^2 + R_3^2 + H^2\right)^2 - \left(2R_2R_3\right)^2} \\ & - \sqrt{\left(R_2^2 + R_4^2 + H^2\right)^2 - \left(2R_2R_4\right)^2} \\ & + \sqrt{\left(R_1^2 + R_4^2 + H^2\right)^2 - \left(2R_1R_4\right)^2} \\ & - \sqrt{\left(R_1^2 + R_3^2 + H^2\right)^2 - \left(2R_1R_3\right)^2} \Bigg]. \end{aligned} \tag{17}$$

The calculation method for the radiative heat flux from the plasma to the anode surface $q_{r,a}$ (or the radiative heat flux to the cathode surface $q_{r,c}$) used here in sprit is similar to that suggested in [28], but is appreciably different from that employed by the authors of [18]. For calculating the radiation energy flux from the arc column to the anode surface, they considered only the contribution from the plasma region along the line parallel to the arc axis. The second term on the right-hand side of Eq. (15) represents the electron 'condensation' heat and the energy gained by the electrons due to their acceleration by the anode potential drop (V_a). Here j is the local current density obtained from the solution of the electrical potential equation, whereas $W_{s,a}$ and V_a denote respectively, the effective work function of the anode material and the anode potential drop ($W_{s,a} = 4.65$ V and $V_a = 3.0$ V are used here).

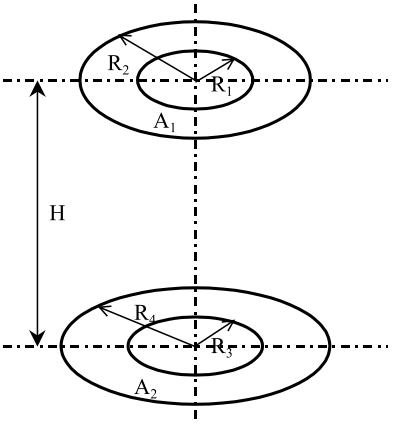

Fig. 2. Schematic diagram used for the derivation of the angle factor.

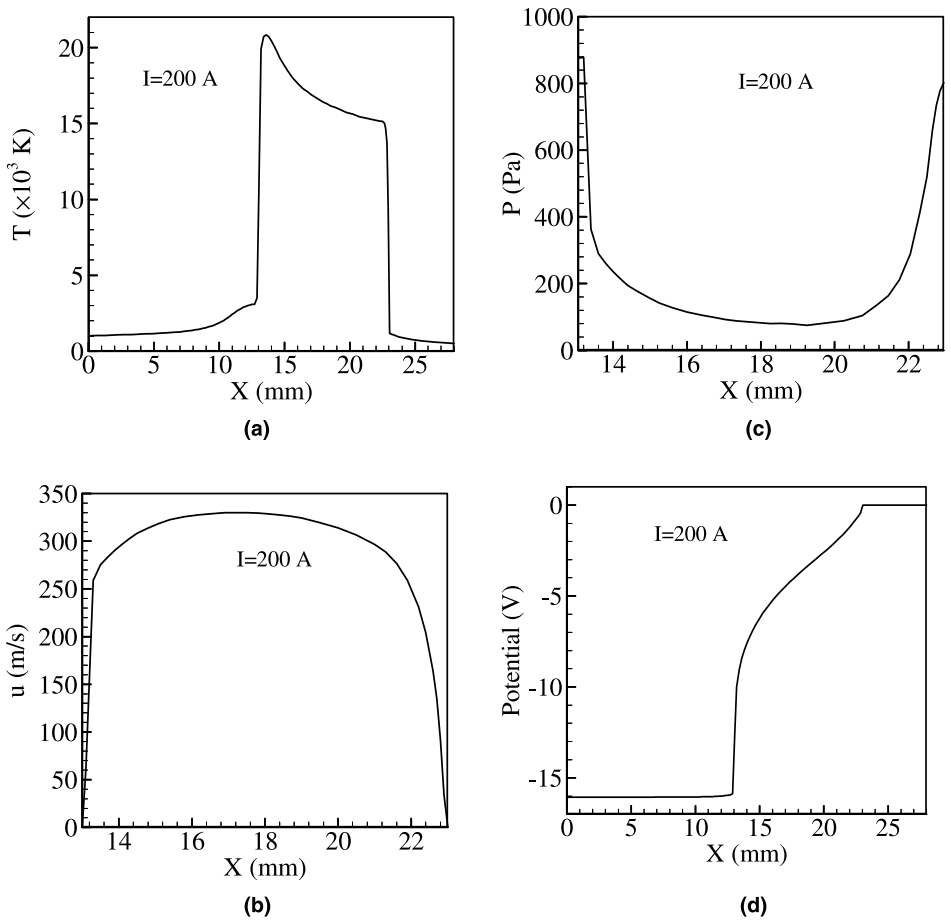

Fig. 3. Computational profiles along the arc axis for the 200 A argon free-burning arc. (a) Temperature profile; (b) axial plasma velocity profile; (c) gas pressure profile; (d) electrical potential profile.

3. Results and discussion

3.1. Predicted results for the 200 A argon arc

The governing equations are solved with the modified SIMPLE-like algorithm (the 'pseudo-density' method and the deferred correction scheme are used for the solution of the energy equation). For the case with the high-intensity free-burning argon arc shown in Fig. 1 with current of 200 A, predicted results are plotted in Figs. 3–5.

The variations of the temperature, axial plasma velocity, gas pressure and electric potential along the arc axis are plotted in Fig. 3(a)–(d), respectively. The predicted maximum temperature of the cathode tip is about 3489 K, which is lower than the melting point of the thoriated tungsten. This maximum temperature is considerably different from that reported by Lowke et al. [19] and by Menart and Lin [13]. The possible reason is that different values of the work function of cathode

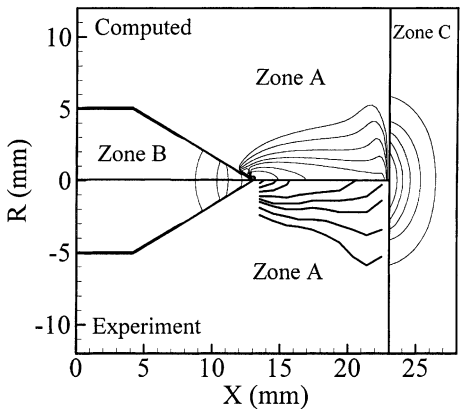

Fig. 4. Comparison of the computed isotherms (upper half) with the experimental data (lower half; from Hsu et al. [1]) for the 200 A argon free-burning arc. Outer isotherm, 11 000 K, interval 1000 K for the temperature range 11 000–15 000 K, whereas interval 2000 K is for the temperature range 15 000–21 000 K.

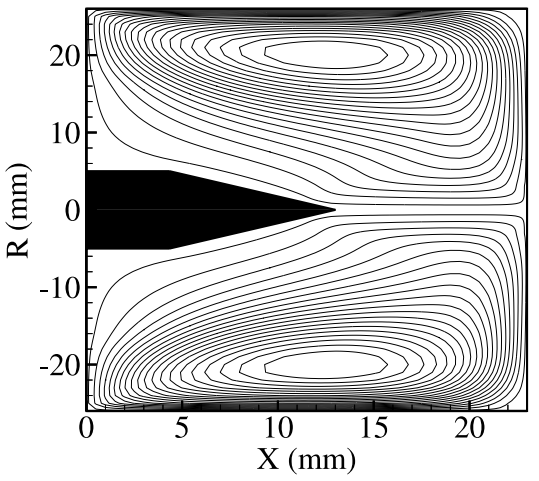

Fig. 5. Computed streamlines for the 200 A argon free-burning arc.

material and different treatments at the cathode–plasma interface were used in those studies. In the downstream region of the cathode tip, the cold gas entrained into the arc is heated strongly by the Joule heating and the gas temperature increases rapidly. The highest value of the plasma temperature predicted in this computation is 20 806 K which is close to the measured value 21 000 K by Hsu et al. [1]. With the increase of the distance from the cathode tip, the plasma temperature decreases due to the continuous mixing of the plasma with the entrained gas and drops rapidly near the cold anode surface (Fig. 3(a)). The maximum temperature within the water-cooled anode plate is 1212 K, which is lower than the melting point of the copper.

Near the cathode tip, the cold gas is entrained into the arc region from the surroundings by the Maecker effect. The gas is heated strongly and expands rapidly associated with a rapid increase of the axial velocity, resulting in the formation of the cathode jet. The predicted maximum axial velocity is 328 m/s. When the plasma jet approaches the anode, the axial velocity decreases rapidly (Fig. 3(b)) in association with the rapid increase of the pressure (Fig. 3(c)) because of the obstacle of the anode and the turning of the flow direction. The plasma is forced to flow toward the r-direction near the anode plate.

The electrical potential drop in the bulk plasma is comparatively small. Near the cathode or anode, an appreciable electrical potential drop appears since the plasma temperatures are comparatively low near the cold electrode surfaces. The potential gradients become very small within the electrode zones because of the rather great values of the electrical conductivity of the electrode materials (Fig. 3(d)). The predicted total potential difference between the anode and the cathode is 16.1 V, which is slightly less than the measured arc voltage 16.9 V reported by Etemadi and Pfender [29].

Fig. 4 compares the computed isotherms with the spectrometrically measured results of Hsu et al. [1]. In the plasma region (Zone A), the predicted isotherms plotted in this figure above the arc axis are in reasonable agreement with the experimental data shown below the axis. The predicted isotherms within the cathode and the anode are also shown in the same figure, but with different temperature scales. Namely, the isotherms within the cathode region (Zone B) correspond to 1000 K (left line) to 3000 K with the interval of 500 K, whereas the isotherms within the anode plate (Zone C) are from 600 K (right line) to 1000 K with the interval of 100 K.

The streamlines within the flow region are plotted in Fig. 5. A large recirculation vortex is seen in this figure, and the rotating direction of the vortex above the axis is counterclockwise.

The calculated maximum value of the axial current density at the plane AD is 2.33×10^8 A/m^2, which is slightly greater than the predicted result 2.29×10^8 A/m^2 in [13], and is appreciably greater than the value of 1.2×10^8 A/m^2 adopted in [1].

3.2. Effect of the potential boundary condition at the rear face of the anode

It is indicated in Section 2.3 that the condition $\phi = 0$ usually employed at the rear face of the anode plate does not always represent the actual cases, since in practice only a part of the rear face is often used as the arc current passage. Some typical computed results are thus presented here to reveal how different boundary conditions at the rear face of the anode plate affect the current density and temperature distributions within the anode plate. Three different cases are considered for the potential boundary conditions at the rear face of the anode (BC). Namely, *Case A*: $\phi = 0$ is used for the annular region with a radius range 15 mm $\leqslant r \leqslant$ 20 mm, whereas $\partial\phi/\partial x = 0$ is used for the other part of BC. *Case B*: $\phi = 0$ is used for the central region with radius $r \leqslant 5$ mm, whereas $\partial\phi/\partial x = 0$ is used for the other part of BC. *Case C*: $\phi = 0$ is used for the whole rear face of the anode plate.

The computed results concerning the current streamlines and the Joule heating-rate contours are plotted in Figs. 6(a)–7(c), respectively for the three different cases.

Examination of the computed results shown in Fig. 6(a)–(c) reveals that different potential boundary conditions at the rear face of the anode plate (BC) almost have no effect on the distributions of the current density within the cathode region and within the arc itself. The current streamlines for the three cases always concentrate to a rather small central region (with

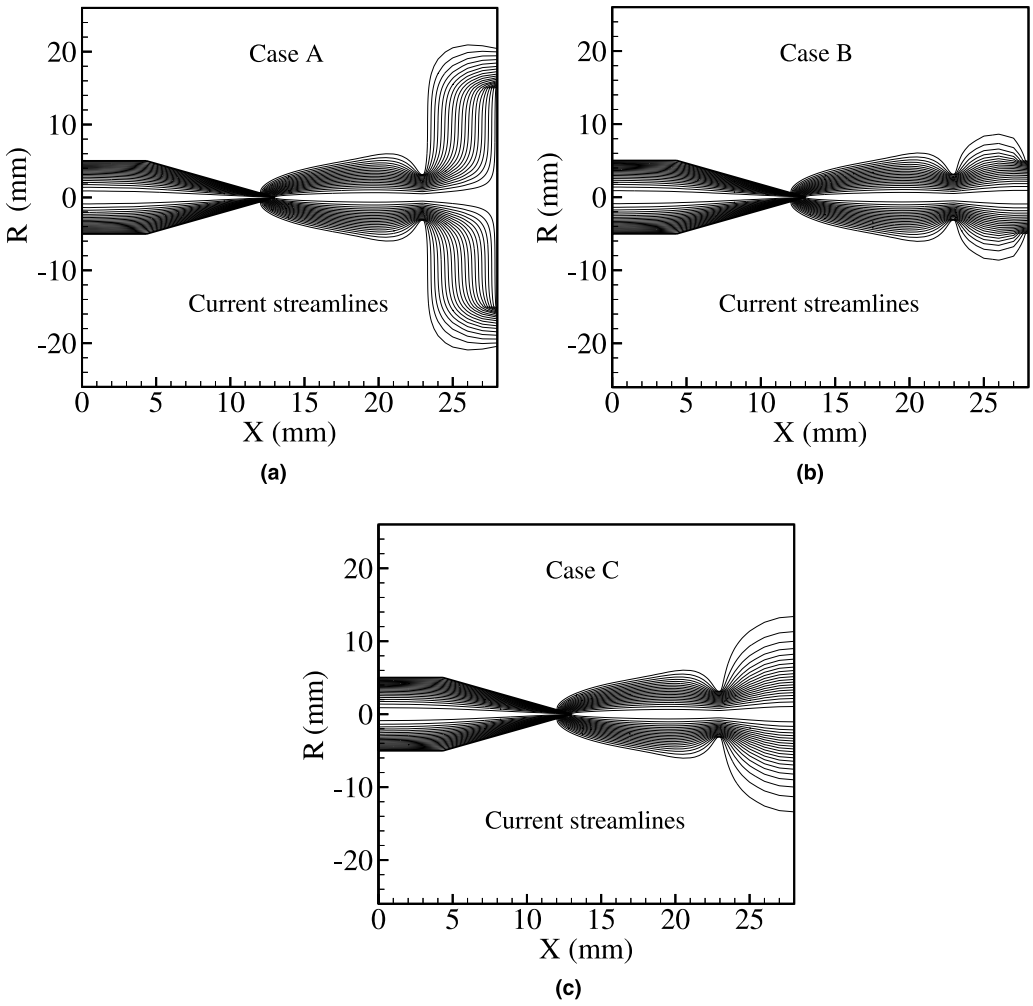

Fig. 6. Computed current streamlines for the 200 A argon free-burning arc and with three different potential boundary conditions at BC. (a) $\phi = 0$ for $15 \leqslant r \leqslant 20$ mm and $\partial\phi/\partial x = 0$ for the other part of BC (*Case A*); (b) $\phi = 0$ for $r \leqslant 5$ mm and $\partial\phi/\partial x = 0$ for the other part of BC (*Case B*); (c) $\phi = 0$ for all the boundary BC (*Case C*).

radius less than 5 mm for the 200 A argon arc) on the frontal face of the anode plates. Correspondingly, the Joule heating-rate contours also remain almost the same within the cathode region and the arc region, as seen from Fig. 7(a)–(c). On the other hand, the potential boundary conditions at the rear face of the anode plate (BC) can affect appreciably the distributions of the current density within the anode plate, as seen in Fig. 6(a)–(c). As a result, the potential boundary conditions at BC affect the Joule heating rate distribution shown in Fig. 7(a)–(c) and affect the temperature field (Fig. 8) within the anode plate to some extent. These results may be of significance for the simulation of the arc weld pools and other applications involving the heating, melting and/or evaporation of anode materials [22].

3.3. Effect of the special treatment at the plasma–anode interface

The net local energy flux from the plasma to the anode surface includes the contribution due to convection, radiation and the electron acceleration and 'condensation'. The local heat flux obtained from the solution of the governing equations is only the part due to the convection, and thus an additional energy flux given by Eq. (15) should be adopted on the anode surface. This energy flux, after conversion mentioned above, is used as the additional source term for the energy equation in the near-surface control volumes in the anode side. In the computation it is found that the radiation heat loss from the anode surface is negligible, but each of the two terms given in Eq. (15) cannot be

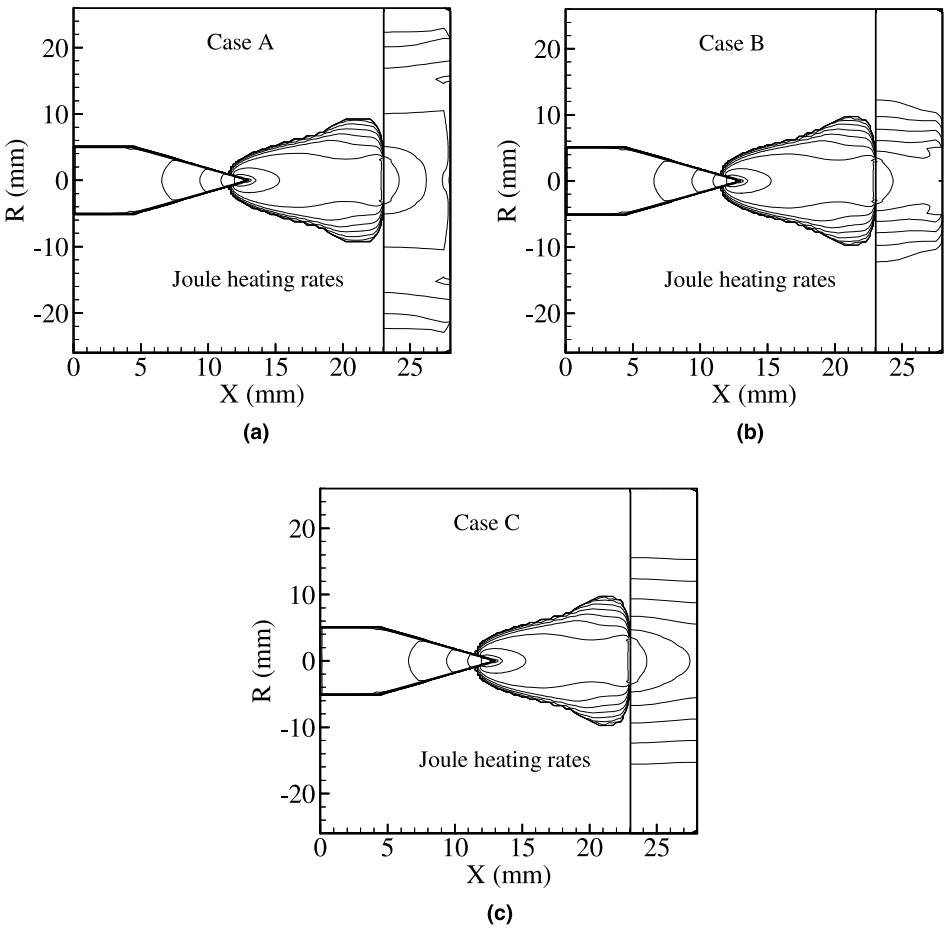

Fig. 7. Computed Joule heating rate contours for the 200 A argon free-burning arc and with three different potential boundary conditions at BC. The maximum is located near the cathode tip with value 10^{12} W/m^3 and the value ratio for two adjacent lines is 10. (a) $\phi = 0$ for $15 \leqslant r \leqslant 20$ mm and $\partial\phi/\partial x = 0$ for the other part of BC (*Case A*); (b) $\phi = 0$ for $r \leqslant 5$ mm and $\partial\phi/\partial x = 0$ for the other part of BC (*Case B*); (c) $\phi = 0$ for all the boundary BC (*Case C*).

neglected in comparison with that due to convection. Our numerical results show that 68.6% of the total heat flux from the plasma to the anode can be attributed to the convection, 23.7% to the electron condensation and acceleration, whereas 7.7% is due to the radiation from the plasma to the anode surface. Some typical calculated results are shown in Fig. 9 concerning the temperature profiles within the anode plates along the axis. Three different cases are considered in the computation: (I) Both the additional terms due to the radiation from the plasma to the anode surface and due to the current density, given in Eq. (15), are included. (II) The radiation heat transfer from the plasma to the anode surface is ignored, whereas the additional term associated with the current density is retained. (III) Both the additional energy flux terms are ignored. It can be seen from Fig. 9 that including each of the additional terms at the plasma–anode interface is important for calculating the temperature distribution within the anode plate.

Plasma sheaths are treated in a simplified way and the plasma has been assumed to be optically thin in the present modeling, as in most of the previous studies. Many complicated factors, especially those associated with the plasma sheaths and the radiation energy transport, which may affect the arc behavior [30–32], are not included in this study. Including radiation energy transport and/or detailed plasma sheaths will make the arc modeling much more complicated, but certainly represent a further improvement.

4. Conclusions

An improved modeling approach concerning the high-intensity free-burning arc has been proposed and used in the present study. Main conclusions obtained are as follows:

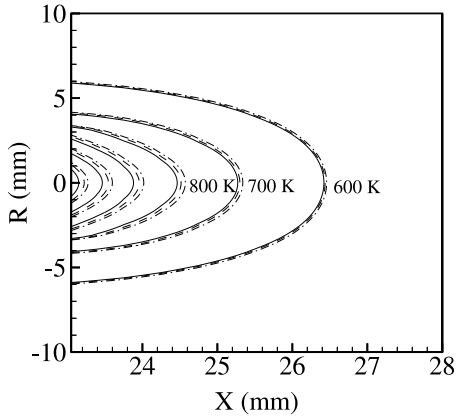

Fig. 8. Computed temperature distributions within the anode plate for three different potential boundary conditions at BC. Solid line – *Case A*; dash line – *Case B*; dotted line – *Case C*.

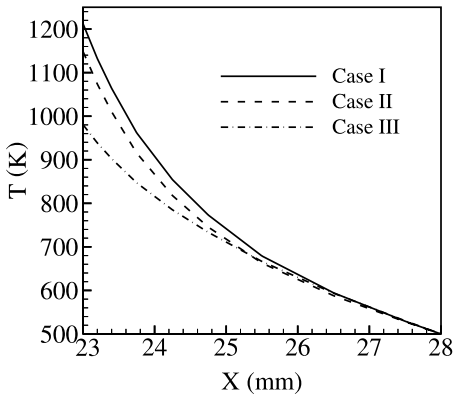

Fig. 9. Computed temperature profiles within the anode plate along the axis for three different additional treatments at the plasma–anode interface. Solid line – both the radiation and current terms are included (*Case I*); dash line – with the current term but without the radiation term (*Case II*); dotted line – both the radiation and current terms are ignored (*Case III*).

1. In order to obtain physically correct heat fluxes from the plasma to the electrode surfaces, the energy equation with temperature as the dependent variable should be used. In addition, one has to pay close attention to the solution of this energy equation. In this study, the energy equation has been solved successfully by using the 'pseudo-density' method and the deferred-correction scheme for the convection term.
2. Different potential boundary conditions at the rear face of the anode plate almost have no effect on the current streamlines in the cathode or within the arc itself, but affect the current density and the temperature distributions within the anode plate.
3. When the unified computational domain including the arc and the cathode and anode is used, additional treatments are required at the plasma–electrode interfaces to consider the additional energy fluxes at the electrode surfaces. The radiative heat flux from the plasma region to the anode surface is shown to be non-negligible.
4. The predicted isotherms for a 200 A argon free-burning arc agree reasonably with corresponding experimental data.

Acknowledgements

This study was supported by the National Natural Science Foundation (grant No. 59836220) and by the Basic Study Fund of Tsinghua University.

References

[1] K.C. Hsu, K. Etemadi, E. Pfender, Study of the free-burning high-intensity argon arc, J. Appl. Phys. 54 (3) (1983) 1293–1301.
[2] S.V. Patankar, Numerical Heat Transfer and Fluid Flow, McGraw-Hill, New York, 1980.
[3] P. Kovitya, L.E. Cram, A two-dimensional model of gas-tungsten welding arcs, Welding J. 65 (12) (1986) 34–39.
[4] G.Y. Zhao, M. Dassanayake, K. Etemadi, Numerical simulation of a free-burning argon arc with copper evaporation from the anode, Plasma Chem. Plasma Process. 10 (1) (1990) 87–98.
[5] M. Suzuki, Y. Sato, H. Akatsuka, Numerical analysis of the behavior of hydrogen added into a free-burning arc, Plasma Chem. Plasma Process. 16 (3) (1996) 399–415.
[6] M. Cao, P. Proulx, M.I. Boulos, J. Mostaghimi, Mathematical modeling of high-power transferred arcs, J. Appl. Phys. 76 (12) (1994) 7757–7767.
[7] R. Westhoff, J. Szekely, A model of fluid, heat flow, and electromagnetic phenomena in a nontransfered arc plasma torch, J. Appl. Phys. 70 (7) (1991) 3455–3466.
[8] P. Kovitya, J.J. Lowke, Two-dimensional analysis of free burning arcs in argon, J. Phys. D: Appl. Phys. 18 (1) (1985) 53–70.
[9] P. Zhu, J.J. Lowke, R. Morrow, A unified theory of free burning arcs, cathode sheaths and cathodes, J. Phys. D: Appl. Phys. 25 (8) (1992) 1221–1230.
[10] J.J. Lowke, P. Kovitya, H.P. Schmidt, Theory of free-burning arc columns including the influence of the cathode, J. Phys. D: Appl. Phys. 25 (11) (1992) 1600–1606.
[11] H.-P. Schmidt, G. Speckhofer, Experimental and theoretical investigation of high-pressure arcs. Part I: the cylindrical arc column (two-dimensional modeling), IEEE Trans. Plasma Sci. 24 (4) (1996) 1229–1238.
[12] G. Speckhofer, H.-P. Schmidt, Experimental and theoretical investigation of high-pressure arcs. Part II: the magnetically deflected arc (three-dimensional modeling), IEEE Trans. Plasma Sci. 24 (4) (1996) 1239–1248.
[13] J. Menart, L. Lin, Numerical study of high-intensity free-burning arc, J. Thermopysics Heat Transfer 12 (4) (1998) 500–506.

[14] J. Menart, L. Lin, Numerical study of a free-burning argon arc with copper contamination from the anode, Plasma Chem. Plasma Process. 19 (1) (1999) 153–170.
[15] J.J. Gonzalez, A. Gleizes, P. Proulx, M. Boulos, Mathematical modeling of a free-burning arc in the presence of metal vapor, J. Appl. Phys. 74 (5) (1993) 3065–3070.
[16] A. Gleizes, M. Bouaziz, J.-J. Gonzalez, M. Razafinimanana, Influence of the anode material on an argon arc, IEEE Trans. Plasma Sci. 25 (5) (1997) 891–896.
[17] A. Kaddani, C. Delalondre, O. Simonin, H. Minoo, Thermal and electrical coupling of arc electrodes, High Temp. Chem. Process. 3 (1994) 441–448.
[18] P. Zhu, J.J. Lowke, R. Morrow, J. Haidar, Prediction of anode temperatures of free burning arcs, J. Phys. D: Appl. Phys. 28 (7) (1995) 1369–1376.
[19] J.J. Lowke, R. Morrow, J. Haidar, A simplified unified theory of arcs and their electrodes, J. Phys. D: Appl. Phys. 30 (14) (1997) 2033–2042.
[20] J.P. Van Doormaal, G.D. Raithby, Enhancement of the SIMPLE method for predicting incompressible fluid flows, Numer. Heat Transfer 7 (2) (1984) 147–163.
[21] M.P. Collares, E. Pfender, Effect of current connection to the anode nozzle on plasma torch efficiency, IEEE Trans. Plasma Sci. 25 (5) (1997) 864–871.
[22] Y. Joshi, P. Dutta, P.E. Schupp, D. Espinosa, Nonaxisymmetric convection in stationary gas tungsten arc weld pools, J. Heat Transfer, Trans. ASME 119 (1) (1997) 164–172.
[23] X. Chen, P. Han, A note on the solution of conjugate heat transfer problems using SIMPLE-like algorithms, Int. J. Heat Fluid Flow 21 (4) (2000) 463–467.
[24] P.K. Khosla, S.G. Rubin, A diagonally dominant second-order accurate implicit scheme, Comput. & Fluids 2 (1974) 207–209.
[25] I. Demirdzic, Z. Lilek, M. Peric, Collocated finite volume method for predicting flows at all speeds, Int. J. Numer. Methods Fluids 16 (12) (1993) 1029–1050.
[26] E.U. Condon, H. Odishaw, Handbook of Physics, second ed., McGraw-Hill, New York, 1967, pp. 8.67–8.84.
[27] M. Ushio, A.A. Sadek, F. Matsuda, Comparison of temperature and work function measurements obtained with different GTA electrodes, Plasma Chem. Plasma Process. 11 (1) (1991) 81–101.
[28] X. Chen, Heat transfer and flow in a radio-frequency plasma torch – a new modelling approach, Int. J. Heat Mass Transfer 33 (5) (1990) 815–826.
[29] K. Etemadi, E. Pfender, Impact of anode evaporation on the anode region of a high-intensity argon arc, Plasma Chem. Plasma Process. 5 (2) (1985) 175–182.
[30] K.-U. Riemann, The Bohm criterion and sheath formation, J. Phys. D: Appl. Phys. 24 (4) (1991) 493–518.
[31] M.S. Benilov, A. Marotta, A model of the cathode region of atmospheric pressure arcs, J. Phys. D: Appl. Phys. 28 (9) (1995) 1869–1882.
[32] M. Tanaka, M. Ushio, C.S. Wu, One-dimensional analysis of the anode boundary layer in free-burning argon arcs, J. Phys. D: Appl. Phys. 32 (5) (1999) 605–611.